The Astrophysical Journal, 809:41 (15pp), 2015 August 10 doi:10.1088/0004-637X/809/1/41

TESTING THEORIES OF GRAVITATION USING 21-YEAR TIMING OF PULSAR BINARY J1713+0747

W. W. Zhu[1,2], I. H. Stairs[1], P. B. Demorest[3], D. J. Nice[4], J. A. Ellis[5,17], S. M. Ransom[6], Z. Arzoumanian[7,8], K. Crowter[1],
T. Dolch[9], R. D. Ferdman[10], E. Fonseca[1], M. E. Gonzalez[1,11], G. Jones[12], M. L. Jones[13], M. T. Lam[9], L. Levin[13,14],
M. A. McLaughlin[13], T. Pennucci[15], K. Stovall[16], and J. Swiggum[13]
[1] Department of Physics and Astronomy, 6224 Agricultural Road, University of British Columbia,
Vancouver, BC, V6T 1Z1, Canada; zhuww@phas.ubc.ca, istairs@phas.ubc.ca
[2] Max-Planck-Institut für Radioastronomie, Aufdem Hügel 69, D-53121, Bonn, Germany
[3] National Radio Astronomy Observatory, P.O. Box 0, Socorro, NM 87801, USA
[4] Department of Physics, Lafayette College, Easton, PA 18042, USA
[5] Jet Propulsion Laboratory, California Institute of Technology, 4800 Oak Grove Dr. Pasadena, CA 91109, USA
[6] National Radio Astronomy Observatory, Charlottesville, VA 22903, USA
[7] Center for Research and Exploration in Space Science and Technology and X-Ray Astrophysics Laboratory,
NASA Goddard Space Flight Center, Code 662, Greenbelt, MD 20771, USA
[8] Universities Space Research Association, Columbia, MD 21046, USA
[9] Department of Astronomy, Cornell University, Ithaca, NY 14853, USA
[10] Department of Physics, McGill University, Montreal, QC H3A 2T8, Canada
[11] Department of Nuclear Medicine, Vancouver Coastal Health Authority, Vancouver, BC V5Z 1M9, Canada
[12] Department of Physics, Columbia University, 550 W. 120th St. New York, NY 10027, USA
[13] Department of Physics and Astronomy, West Virginia University, P.O. Box 6315, Morgantown, WV 26505, USA
[14] Jodrell Bank Centre for Astrophysics, School of Physics and Astronomy, The University of Manchester, Manchester M13 9PL, UK
[15] Department of Astronomy, University of Virginia, P.O. Box 400325 Charlottesville, VA 22904-4325, USA
[16] Department of Physics and Astronomy, University of New Mexico, Albuquerque, NM, 87131, USA

Received 2015 April 2; accepted 2015 July 6; published 2015 August 7

ABSTRACT

We report 21-year timing of one of the most precise pulsars: PSR J1713+0747. Its pulse times of arrival are well modeled by a comprehensive pulsar binary model including its three-dimensional orbit and a noise model that incorporates short- and long-timescale correlated noise such as jitter and red noise. Its timing residuals have weighted root mean square ~92 ns. The new data set allows us to update and improve previous measurements of the system properties, including the masses of the neutron star ($1.31 \pm 0.11\, M_\odot$) and the companion white dwarf ($0.286 \pm 0.012\, M_\odot$) as well as their parallax distance 1.15 ± 0.03 kpc. We measured the intrinsic change in orbital period, $\dot{P}_{\rm b}^{\rm Int}$, is $-0.20 \pm 0.17\ {\rm ps\,s^{-1}}$, which is not distinguishable from zero. This result, combined with the measured $\dot{P}_{\rm b}^{\rm Int}$ of other pulsars, can place a generic limit on potential changes in the gravitational constant G. We found that $\dot{G}/G$ is consistent with zero [$(-0.6 \pm 1.1) \times 10^{-12}\ {\rm yr^{-1}}$, 95% confidence] and changes at least a factor of 31 (99.7% confidence) more slowly than the average expansion rate of the universe. This is the best $\dot{G}/G$ limit from pulsar binary systems. The $\dot{P}_{\rm b}^{\rm Int}$ of pulsar binaries can also place limits on the putative coupling constant for dipole gravitational radiation $\kappa_{\rm D} = (-0.9 \pm 3.3) \times 10^{-4}$ (95% confidence). Finally, the nearly circular orbit of this pulsar binary allows us to constrain statistically the strong-field post-Newtonian parameters Δ, which describes the violation of strong equivalence principle, and $\hat{\alpha}_3$, which describes a breaking of both Lorentz invariance in gravitation and conservation of momentum. We found, at 95% confidence, $\Delta < 0.01$ and $\hat{\alpha}_3 < 2 \times 10^{-20}$ based on PSR J1713+0747.

Key words: binaries: general – gravitation – parallaxes – pulsars: individual (PSR J1713+0747) – stars: neutron

1. INTRODUCTION

We present 21-year timing of the millisecond pulsar (MSP) J1713+0747, which was discovered in 1993 (Foster et al. 1993). It is one of the brightest pulsars timed by the North American Nanohertz Observatory for Gravitational Waves (NANOGrav; Demorest et al. 2013; McLaughlin 2013), and has the smallest timing residual of all NANOGrav pulsars (Demorest et al. 2013). The timing analysis reported in this paper will be incorporated into future pulsar timing array projects. Timing observations of this pulsar were reported previously in Camilo et al. (1994), Lommen & Backer (2001), van Straten & Bailes (2003), Splaver et al. (2005), Hotan et al. (2006), and Verbiest et al. (2009). We report new results that arise from a significant extension of the timing baseline and use of wide-bandwidth, high-resolution instruments that allow us to model and account for pulse time variations due to dispersion in the interstellar medium (ISM; Section 3.2) and small distortions of the pulsar's magnetosphere (Section 3.4).

MSPs are very stable rotators due to their enormous angular momentum. PSR J1713+0747 is an MSP residing in a wide binary orbit with a white dwarf companion (Section 3). The pulse arrival times of the pulsar are well fit by a binary model with a nearly circular orbit. The masses of the binary components can be inferred through the measurement of the mass function and Shapiro delay (Splaver et al. 2005). The system's distance is well-measured through a timing parallax. We detect a changing projected orbital semimajor axis due to the orbit's proper motion on the sky. Through the rate of change of projected semimajor axis, we can infer the orientation of the orbit in the sky. This is one of the few binaries in which the three-dimensional (3D)-orientation of the binary orbit can be completely solved. Using 21 years of data,

---

[17] Einstein Fellow.

Table 1
21 Year J1713+0747 Observations

System	Alias[a]	Observatory	Dates	Number of ToAs	Epochs	Bandwidth (MHz)	Typical Integration Time (minutes)
Mark III-A[b](1410 MHz)	M3A-L	Arecibo	1992 Jun–1993 Jan	9	9	40	47
Mark III-B[c](1410 MHz)	M3B-L	Arecibo	1993 Jan–1994 Jan	46	46	40	47
Mark IV (1410 MHz)	M4-L	Arecibo	1998 Jul–2004 May	81	81	10	58
Mark IV (2380 MHz)	M4-S	Arecibo	1999 Oct–2004 May	44	44	10	29
Mark IV-O[d] (1410 MHz)	M4O-L	Arecibo	2004 Jun–2005 Mar	22	16	10	60
Mark IV-O[d] (2380 MHz)	M4O-S	Arecibo	2004 Jun–2005 Jan	8	7	10	30
ABPP (1410 MHz)	ABPP-L	Arecibo	1998 Feb–2004 May	98	89	56	60
ABPP (2380 MHz)	ABPP-S	Arecibo	1999 Dec–2004 May	46	46	112	30
ASP (1410 MHz)	ASP-L	Arecibo	2005 Jan–2012 Jan	990	48	64	20
ASP (2350 MHz)	ASP-S	Arecibo	2005 Jan–2012 Mar	668	41	64	20
GASP (800 MHz)	GASP-8	GBT	2006 Mar–2011 Jan	997	41	64	20
GASP (1410 MHz)	GASP-L	GBT	2006 Mar–2010 Jun	863	42	64	20
GUPPI (800 MHz)	GUPPI-8	GBT	2010 Mar–2013 Oct	3533	49	800	20
GUPPI (1410 MHz)	GUPPI-L	GBT	2010 Mar–2013 Nov	4381	64	800	20
PUPPI (1410 MHz)	PUPPI-L	Arecibo	2012 Mar–2013 Nov	1972	26	800	20
PUPPI (2300 MHz)	PUPPI-S	Arecibo	2012 Mar–2013 Nov	992	24	800	20

Notes.
[a] These short names are used in Figures 1 and 2 and Table 4.
[b] Filter bank used a 78 μs time constant.
[c] Filter bank used a 20 μs time constant.
[d] Here Mark IV-O stands for the recently processed Mark IV data that partially overlap with ASP data.

we refine the previously published measurements of these orbital parameters. We observed apparent variation of the binary orbital period due to the Shklovskii effect and Galactic differential acceleration. We also find a stringent constraint on the intrinsic variation of the orbital period, which enable us to test alternative theories of gravitation.

The stability and long orbital period of the PSR J1713+0747 binary make it an excellent laboratory for observing the time variation of Newton's gravitational "constant" G. This interesting conjecture of G varying on a cosmological timescale was first raised by Dirac (1937) based on his large-number hypothesis. Later this become a prediction of some alternative theories of gravitation. For example, the scalar-tensor theory (Jordan 1955, 1959; Fierz 1956; Brans & Dicke 1961) modifies Einstein's equation of gravitation by coupling mass with long-range scalar-tensor fields, and predicts that, as the universe expands, the scalar field will also change, causing the effective gravitational constant to vary on the cosmological timescale. Similar ideas were also revisited by gravitational theories involving extra dimensions (Marciano 1984; Wu & Wang 1986). PSR J1713+0747 is likely the best pulsar binary for testing the constancy of G thanks to its high timing precision and long orbital period. Using timing results reported in this paper, we found a stringent generic upper limit on $\dot{G}$ (see Section 4.3 for details).

The PSR J1713+0747 binary is also an excellent laboratory for testing the strong equivalence principle (SEP) and the preferred frame effect (PFE; in this work, we constrain the putative post-Newtonian parameter $\hat{\alpha}_3$ that characterizes a specific type of PFE; for details see Section 4.4). The violation of SEP or the existence of non-zero $\hat{\alpha}_3$ could lead to potentially observable effects which cannot be accounted in the context of GR, such as forced-polarization of the binary orbit. Some of these effects are discussed in Freire et al. (2012a) and Will (2014). We can put stringent generic constraints on alternative theories by observing low-eccentricity pulsar binary systems. Section 4.4 presents the constraint on the violation of SEP and the significance of $\hat{\alpha}_3$ from our 21 years of observation of PSR J1713+0747.

2. OBSERVATIONS

2.1. Data Acquisition Systems

Our data set consists of pulse timing observations of PSR J1713+0747 at the Arecibo Observatory, from 1992 through 2013, and at the Robert C. Byrd Green Bank Telescope (GBT), from 2006 through 2013, using several generations of data acquisition systems as described below (Table 1). The first 12 yr of these data (1992 August through 2004 May) were previously reported by Splaver et al. (2005) using the Mark III, Mark IV, and Arecibo-Berkeley Pulsar Processor (ABPP) systems. In this work, we incorporate an extension of the Mark IV data set (reduced using the same process as Splaver et al. 2005); data collected at Arecibo from two newer systems; and data collected at the GBT.

The earliest observations (Mark III) were made using a single receiver operating over a limited bandwidth, and hence intrinsic pulsar behavior cannot be separated from effects of the ISM. Subsequent observations at both telescopes were made using two receivers at widely spaced frequencies (1410 and 2380 MHz at Arecibo; 800 and 1410 MHz at the GBT) to allow for separation of these effects.

The earliest observations (1992–1994) used the Princeton Mark III (Stinebring et al. 1992), which collected dual-polarization data with a filter bank of 32 spectral channels each 1.25 MHz wide. Observations between 1998 and 2004 used the Princeton Mark IV (Stairs et al. 2000) instrument and the ABPP (Backer et al. 1997) system in parallel. The Mark IV system collected 10 MHz passband data using 2 bit sampling. The data were coherently dedispersed and folded at the pulse period offline. The ABPP system sampled voltages with 2 bit resolution and filtered the passband into 32 spectral channels

(1.75 MHz per channel and 56 MHz in total for 1410 MHz band; 3.5 MHz per channel and 112 MHz in total for 2380 MHz band), and applied coherent dedispersion to each channel using 3 bit coefficients.

From 2004 to 2011/12, pulsar data were collected with the Astronomical Signal Processor (ASP; Demorest 2007) and its Green Bank counterpart GASP (Demorest 2007). The (G)ASP systems recorded 8 bit sampled ~64 MHz bandwidth data and applyed real-time coherent dedispersion and pulse period folding. The resulting data contain 2048-bin full-Stokes pulse profiles integrated over 1–3 minutes. When observing with ASP we used 16 channels each 4 MHz wide between 1440 and 1360 MHz, and 16 channels between 2318 and 2382 MHz. When observing with GASP we used 12 channels between 1386 and 1434 MHz, and 16 channels between 822 and 886 MHz. The J1713+0747 ASP/GASP data were also reported in Demorest et al. (2013).

We started using the Green Bank Ultimate Pulsar Processing Instrument (GUPPI; DuPlain et al. 2008) for GBT observations in 2010 and its clone the Puerto-Rican Ultimate Pulsar Processing Instrument (PUPPI) for Arecibo observations in 2012. GUPPI and PUPPI use 8 bit sampling in real-time coherent dedispersion and pulse period folding mode and produce 2048-bin full-Stokes pulse profiles integrated over 10 second intervals. When observing with the 800 MHz receiver at the GBT, we use GUPPI to collect data from 62 spectral channels each 3.125 MHz wide, covering 724–918 MHz in frequency. With the L-band receiver, GUPPI uses 58 spectral channels each 12.5 MHz wide, covering the 1150–1880 MHz band. When observing with the L-band receiver at Arecibo, we use PUPPI to collect data from 1150–1765 MHz using 50 spectral channels each 12.5 MHz wide. When observing with the S band, PUPPI takes data from 1770–1880 MHz and 2050–2405 MHz using 38 spectral channels each 12.5 MHz wide. The spectral bandwidth and resolution provided by GUPPI and PUPPI are crucial for resolving the pulse profile evolution in frequency described in Section 3.4.

2.2. Arrival Time Calculations

We combine the pulse times of arrivals (TOAs) used in Splaver et al. (2005) and those of the later observations, for a data span of 21 years, with a noticeable gap between 1994 and 1998, during the Arecibo upgrade. We used daily averaged TOAs from Splaver et al. (2005), because the original 190 s integration TOAs are not accessible. Data timestamps are derived from observatory masers and retrocorrected to universal Coordinated Time via GPS and then further corrected to the TT(BIPM) timescale using the 2012 version BIPM clock corrections with extrapolations to 2013. The TOAs are measured from the observational data through a series of steps. First the data are folded, as they were being taken, into pulse profiles using an ephemeris known to be good enough for predicting the pulse period for the duration of the observation. The folded profiles from different frequency channels and sub-integrations are often summed together to improve the signal-to-noise ratio of the profiles. Orthogonal polarizations are summed to produce a total-intensity profile. The summed profiles are then compared with a well-measured standard pulse profile from the appropriate frequency band. We employ frequency-domain cross-correlation techniques (Taylor 1992) to determine the phase of the pulse peak relative to the midpoint of the observation. The final TOA of a summed profile is then calculated by adding the mid-observation time and the product of pulse period and the measured peak phase. The flux density of the pulsar in these observations can also be measured by comparing the signal strength in the data with that of a calibration observation taken right before or after the pulsar observation in which a signal with known strength was injected. For the post-upgrade Arecibo data and all the GBT data, the flux density of the calibration signal is calibrated every month by comparing it with an astronomical object of known and constant flux density, in this case, the AGNs J1413+1509 and B1442+09.

2.3. Instrumental Offsets

The telescopes and data acquisition systems introduce varying degrees of computational and electronic delays into the measured TOAs. Further, in many cases, different standard pulse profiles were used to create TOAs from different data acquisition systems. As a result, the TOAs from different systems differ by small time offsets. When a transition is made from one system to another at a telescope, data are typically collected in parallel during a period of around a year, and those data are used to measure the offset between data taken with the instruments. Here we describe the measured offsets in more detail.

There was no overlap between data taken with Mark III (through 1994) and data taken with Mark IV and ABPP (beginning in 1998). The offset between these two systems was treated as a free parameter when fitting timing solutions to the full data set.

Mark IV and ABPP were used in parallel for J1713+0747 observations between 1998 and 2004. They collected data with different bandwidths (Table 1) and were computed using different profile templates. To align the ABPP ToAs with Mark IV, we fitted a phase offset between the 1410 MHz TOAs of the two instruments, and found that ABPP ToAs trail those of Mark IV by 0.46791 ± 0.00009 in pulse phase. In the timing modeling, we fix the phase offsets between Mark IV and ABPP to this value in both 1410 and 2300 MHz, and fit an extra time offset for 2300 MHz ABPP TOAs to account for any extra template misalignment.

Mark IV/ABPP and ASP were used in parallel for several epochs. We fit across the overlap data to determine the offset between the 1410 MHz TOAs of these data sets to measure an offset of $2.33 \pm 0.10\,\mu$s (Mark IV trailing ASP). The offset between the 2300 MHz TOAs of Mark IV and ASP is treated as a free parameter in the full timing solution.

For the offsets between ASP and PUPPI at Arecibo, and GASP and GUPPI at the GBT, analysis of simultaneous observations of many pulsars, including both pulsar signals and radiometer noise, were used to measure very precise offsets between the instruments at each observatory; details will be given in a forthcoming paper (Arzoumanian et al. 2015). Further, the same standard pulse profiles were used in any given band. Thus these data sets form a continuous 9-year collection of TOAs with no arbitrary offsets.

Finally, the offset between the Arecibo 1410 MHz TOAs and GBT Bank 1410 MHz TOAs was treated as a free parameter when fitting timing solutions to the full data set. The offset between the 800 and 1410 MHz GBT TOAs and the offset between the 1410 and the 2300 MHz Arecibo TOAs are also fitted as free parameters.

Table 2
Timing Model Parameters[a] from *TEMPO*

Parameter	EFAC and EQUAD	With Jitter Model	Jitter and Red Noise Model
Measured Parameters			
R.A., α (J2000)	17:13:49.5320251(5)	17:13:49.5320248(7)	17:13:49.5320252(8)
decl., δ (J2000)	7:47:37.506131(12)	7:47:37.506155(19)	7:47:37.50614(2)
Spin frequecy ν (s^{-1})	218.81184385472585(6)	218.81184385472594(10)	218.8118438547251(9)
Spin down rate $\dot{\nu}$ (s^{-2})	$-4.083889(4) \times 10^{-16}$	$-4.083894(7) \times 10^{-16}$	$-4.08382(5) \times 10^{-16}$
Proper motion in α, $\mu_\alpha = \dot{\alpha}\cos\delta$ (mas yr^{-1})	4.9177(11)	4.9179(18)	4.917(2)
Proper motion in δ, $\mu_\delta = \dot{\delta}$ (mas yr^{-1})	−3.917(2)	−3.915(3)	−3.913(4)
Parallax, ϖ (mas)	0.858(15)	0.84(3)	0.85(3)
Dispersion measure[b] (pc cm^{-3})	15.9700	15.9700	15.9700
Orbital period, P_b (day)	67.82513682426(16)	67.82513826935(19)	67.82513826930(19)
Change rate of P_b, $\dot{P}_b$ (10^{-12} s s^{-1})	0.23(12)	0.41(16)	0.44(17)
Eccentricity, e	0.0000749394(3)	0.0000749399(6)	0.0000749402(6)
Time of periastron passage, T_0 (MJD)	53761.03227(11)	53761.0328(3)	53761.0327(3)
Angle of periastron[c], ω (deg)	176.1941(6)	176.1967(15)	176.1963(16)
Projected semimajor axis, x (lt-s)	32.34242243(5)	32.34242188(14)	32.34242188(14)
sin i, where i is the orbital inclination angle	0.9672(11)	0.951(4)	0.951(4)
Companion mass, M_c ($M_\odot$)	0.233(4)	0.287(13)	0.286(13)
Apparent change rate of x, $\dot{x}$ (lt-s s^{-1})	0.00637(7)	0.00640(10)	0.00645(11)
Profile frequency dependency parameter, FD1	−0.00016317(19)	−0.0001623(2)	−0.00016(3)
Profile frequency dependency parameter, FD2	0.0001357(3)	0.0001350(3)	0.00014(3)
Profile frequency dependency parameter, FD3	−0.0000664(6)	−0.0000668(6)	−0.000067(17)
Profile frequency dependency parameter, FD4	0.0000147(4)	0.0000153(4)	0.000015(5)
Fixed Parameters			
Solar system ephemeris	DE421	DE421	DE421
Reference epoch for α, δ, and ν (MJD)	53729	53729	53729
Solar wind electron density n_0 (cm^{-3})	0	0	0
Rate of periastron advance, $\dot{\omega}$ (deg yr^{-1})[d]	0.00020	0.00024	0.00024
Position angle of ascending node, Ω (deg)[e]	88.43	88.43	88.43
Red noise amplitude (μs $year^{1/2}$)	…	…	0.025[f]
Red noise spectral index, γ_{red}	…	…	−2.92
Derived Parameters			
Intrinsic period derivative, $\dot{P}_{Int}$(s s^{-1})[g]	$8.966(12) \times 10^{-21}$	$8.98(2) \times 10^{-21}$	$8.97(2) \times 10^{-21}$
Dipole magnetic field, B (G)[g]	$2.0485(14) \times 10^{8}$	$2.050(3) \times 10^{8}$	$2.049(3) \times 10^{8}$
Characteristic age, τ_c (year)[g]	$8.076(11) \times 10^{9}$	$8.07(2) \times 10^{9}$	$8.07(2) \times 10^{9}$
Pulsar mass, M_{PSR} ($M_\odot$)	0.97(3)	1.32(11)	1.31(11)

Notes.

[a] We used a modified DD binary model (Damour & Deruelle 1986) that allows us to assume a position angle of ascending node (Ω) and fit for the apparent change rate of the projected semimajor axis ($\dot{x}$) due to proper motion. Numbers in parentheses indicate the 1σ uncertainties on the last digit(s). Uncertainties on parameters are estimated by the *TEMPO* program using information in the covariance matrix.

[b] The averaged DM value; see Section 3.2 and Figure 2 for more discussion.

[c] See Figure 2 of Splaver et al. (2005) for definition.

[d] The rate of periastron advance was not fitted but fixed to the GR value because it is highly co-variant with the orbital period.

[e] We optimized Ω using a grid search and held it fix to the value that minimized χ^2.

[f] The value corresponds to 8.7×10^{-15} in the dimensionless strain amplitude unit.

[g] These parameters are corrected for Shklovskii effect and Galactic differential accelerations.

The date span, number of observation epochs, and specifications of the systems are listed in Table 1.

3. TIMING MODEL

We employed the pulsar timing packages TEMPO[18] and TEMPO2 (Hobbs et al. 2006) to model the TOAs.

The rotation of the pulsar was modeled with a low-order polynomials expansion of spin frequency ν and $\dot{\nu}$ (Tables 2 and 3) in order to account for the pulsar's spin and spin down.

The pulsar's position (α, δ) and proper motion (μ_α, μ_δ) on the sky and its parallax ϖ were also measured through timing modeling. The distance inferred from our parallax measurement is $D_{PSR} = 1.15 \pm 0.03$ kpc. This distance is consistent with the VLBA parallax distance of 1.05 ± 0.06 kpc (Chatterjee 2009).

We employed the Damour & Deruelle (1986) (DD) model of binary motion to fit for the binary parameters, including the mass of the white dwarf (M_c) measured through Shapiro delay (Section 4.1), the orbital period P_b, angle of periastron ω, time of periastron passage T_0, projected semimajor axis x and its change rate $\dot{x}$ due to proper motion of the orbit. We observed an apparent $\dot{x}$ as the projection angle of the orbit changed over time due to the perpendicular part of the binary's motion to our line of sight. This allowed us to determine the orientation of the orbit in the sky when combined with the system's proper motion. The orientation of the orbit in the sky is modeled by the parameter Ω, the position angle of the ascending node.

---

[18] http://tempo.sourceforge.net

Table 3
Timing Model Parameters[a] from TEMPO2

Parameter	EFAC and EQUAD	With Jitter Model	Jitter and Red Noise Model
Measured Parameters			
R.A., α (J2000)	17:13:49.5320254(5)	17:13:49.5320247(7)	17:13:49.5320261(10)
decl., δ (J2000)	7:47:37.506130(13)	7:47:37.506130(19)	7:47:37.50615(3)
Spin Frequecy ν (s^{-1})	218.81184385472573(6)	218.81184385472589(10)	218.8118438547255(5)
Spin down rate $\dot{\nu}$ (s^{-2})	$-4.083883(5) \times 10^{-16}$	$-4.083892(7) \times 10^{-16}$	$-4.08386(5) \times 10^{-16}$
Proper motion in α, $\mu_\alpha = \dot{\alpha} \cos \delta$ (mas yr^{-1})	4.9161(12)	4.9181(18)	4.915(3)
Proper motion in δ, $\mu_\delta = \dot{\delta}$ (mas yr^{-1})	−3.915(2)	−3.910(3)	−3.914(5)
Parallax, ϖ (mas)	0.872(16)	0.83(3)	0.87(3)
Dispersion measure[b] (pc cm^{-3})	15.9700	15.9700	15.9700
Orbital period, P_b (day)[c]	67.8251365449(12)	67.8251383194(16)	67.8251383185(17)
Change rate of P_b, $\dot{P}_b$ (10^{-12} s s^{-1})	0.19(13)	0.39(16)	0.36(17)
Eccentricity, e	0.0000749395(3)	0.0000749400(6)	0.0000749402(6)
Time of periastron passage, T_0 (MJD)	53761.03208(11)	53761.0327(3)	53761.0328(3)
Angle of periastron, ω (deg)	176.1930(6)	176.1963(15)	176.1966(14)
Projected semimajor axis, x (lt-s)	32.34242258(5)	32.34242189(13)	32.34242187(13)
Orbital inclination, i (deg)	76.1(3)	71.9(7)	71.9(7)
Companion Mass, M_c ($M_\odot$)	0.222(4)	0.286(13)	0.286(12)
Position angle of ascending node, Ω (deg)	74.3(14)	89.6(20)	88(2)
Profile frequency dependency parameter, FD1	−0.0001634(2)	−0.0001628(2)	−0.0001628(2)
Profile frequency dependency parameter, FD2	0.0001358(3)	0.0001355(3)	0.0001355(3)
Profile frequency dependency parameter, FD3	−0.0000658(6)	−0.0000671(6)	−0.0000672(6)
Profile frequency dependency parameter, FD4	0.0000141(4)	0.0000154(4)	0.0000155(4)
Fixed Parameters			
Solar system ephemeris	DE421	DE421	DE421
Reference epoch for α, δ, and ν (MJD)	53729	53729	53729
Solar wind electron density n_0 (cm^{-3})	0	0	0
Rate of periastron advance, $\dot{\omega}$ (deg yr^{-1})[d]	0.00019	0.00024	0.00024
Red noise amplitude (μs $year^{1/2}$)	…	…	0.025[e]
Red noise spectral index, $\gamma_{\rm red}$	…	…	−2.92
Derived Parameters			
Intrinsic period derivative, $\dot{P}_{\rm Int}$(s s^{-1})[f]	$8.957(13) \times 10^{-21}$	$8.98(2) \times 10^{-21}$	$8.96(2) \times 10^{-21}$
Dipole magnetic field, B(G)[f]	$2.0473(15) \times 10^{8}$	$2.050(3) \times 10^{8}$	$2.048(3) \times 10^{8}$
Characteristic age, τ_c (year)[f]	$8.085(12) \times 10^{9}$	$8.06(2) \times 10^{9}$	$8.08(2) \times 10^{9}$
Pulsar mass, $M_{\rm PSR}$ ($M_\odot$)	0.90(3)	1.31(11)	1.31(11)

Notes.

[a] We used TEMPO2's *T2* binary model, which implicitly account for the changes of the projected semimajor axis, including $\dot{x}$ due to proper motion of the binary (this allows us to fit for the position angle of ascending node, Ω) and the changes due to the orbital parallaxes of the Earth and the pulsar (Kopeikin 1996; Edwards et al. 2006). Numbers in parentheses indicate the 1σ uncertainties on the last digit(s). Uncertainties on parameters are estimated by the TEMPO2 program using information in the covariance matrix. These uncertainties are consistent with the MCMC results using the full nonlinear timing model (Section 3.1), see Figure 5 for examples.

[b] The averaged DM value; see Section 3.2 and Figure 2 for more discussion.

[c] TEMPO2's *T2* model reports the orbital period after correcting for the changes in periastron angle ω due to proper motion and orbital parallaxes. TEMPO DD model does not account for this and therefore reports a slightly different value.

[d] The rate of periastron advance was not fitted but fixed to the GR value because it is highly co-variant with the orbital period.

[e] This value corresponds to 8.7×10^{-15} in the dimensionless strain amplitude unit.

[f] These parameters are corrected for Shklovskii effect and Galactic differential accelerations.

In TEMPO, we grid search for the best Ω and then hold it fixed when fitting other parameters (Table 2). In the T2 model of TEMPO2 (Edwards et al. 2006), Ω is explicitly modeled and fitted, while the changing of x, including the $\dot{x}$ caused by proper motion and the periodic changes due to orbital parallaxes of the Earth and the pulsar (Kopeikin 1996), are implicitly modeled and not fitted as a parameter (Table 3).

In our model, we fixed the orbit's periastron advance rate $\dot{\omega}$ to the value inferred from GR and the best-fit binary parameters (Tables 2, 3). This was done by iteratively updating the values of $\dot{\omega}$ and refitting for new binary parameters many times until the results converged. Fitting for $\dot{\omega}$ as a free parameter resulted in a best-fit value $\gtrsim 3\sigma$ away from the GR prediction. This is likely because, in J1713+0747's nearly circular orbit, $\dot{\omega}$ is strongly covariant with the orbital period $P_{\rm d}$.

Compared with previous timing efforts, we detected, for the first time, an apparent change in the binary period $\dot{P}_b$, which we attribute to the motion of the binary system relative to the Sun. This is described in Section 4.2.

The DMX model was used to fit dispersion measure (DM) variations caused by changes in the ISM along the line of sight (see Section 3.2 for details). The FD model was used to model profile evolution in frequency (see Section 3.4 for details).

In order to account for unknown systematics in TOAs from different instruments, and observation-correlated noise such as pulse jitter noise from pulsar emission process, we employed a general noise model that parameterizes both uncorrelated and

Table 4
Noise Parameters[a] and Residual rms in μs

Backends	$\bar{\sigma}$[b]	EFAC	EQUAD	ECORR	WRMS[c]	AWRMS[d]
All	0.927	⋯	⋯	⋯	0.246	0.092
M3A-L	0.267	⋯	0.599	⋯	0.589	0.588
M3B-L	0.167	⋯	0.412	⋯	0.434	0.432
M4-L	0.172	⋯	0.153	⋯	0.365	0.146
M4-S	0.183	⋯	0.357	⋯	0.668	0.416
M4O-L	0.416	⋯	0.315	⋯	0.324	0.112
M4O-S	0.355	⋯	0.008	⋯	0.277	0.141
ABPP-L	0.106	⋯	0.154	⋯	0.288	0.067
ABPP-S	0.134	⋯	0.260	⋯	0.464	0.303
ASP-L	0.512	0.979	0.035	0.105	0.222	0.073
ASP-S	0.631	1.149	0.004	0.127	0.257	0.115
GASP-8	1.391	1.178	0.000	0.023	0.589	0.098
GASP-L	0.966	1.128	0.040	0.037	0.288	0.080
GUPPI-8	1.550	1.052	0.086	0.204	0.657	0.156
GUPPI-L	0.855	1.204	0.025	0.054	0.266	0.046
PUPPI-L	0.303	1.160	0.001	0.094	0.145	0.075
PUPPI-S	0.653	1.050	0.058	0.114	0.189	0.080

Notes.
[a] The unmodeled EFAC and ECORR values default to 1 and 0, respectively.
[b] The averaged TOA template matching errors $\langle\sigma\rangle$.
[c] Here WRMS is defined as $[(\sum w_i \mathcal{R}_i^2/\sum w_i) - \bar{\mathcal{R}}^2]^{1/2}$, where $\mathcal{R}_i$ is the timing residual of TOA i, $w_i = 1/\sigma_i^2$ is the weight determined by the TOA errors including EFAC and EQUAD, and $\bar{\mathcal{R}} = (\sum w_i \mathcal{R}_i)/\sum w_i$ is the weighted mean of the residuals after removing a red-noise model (as in Figure 1).
[d] AWRMS stands for the weighted rms of epoch-averaged residuals.

correlated noise. The noise modeling is discussed in Section 3.1 and the noise model parameters are listed in Table 4.

We used the JPL DE421 solar system ephemeris (Folkner et al. 2009) to remove pulse time-of-flight variation within the solar system. This ephemeris is oriented to the International Celestial Reference Frame (ICRF) and thus our astrometric results are also given in the ICRF frame. We note parenthetically that a previous generation ephemeris, DE405, gave nearly identical but marginally better timing fits ($\Delta\chi^2 \sim 6$ for 14528 dof in both TEMPO and TEMPO2).

The timing parameters and uncertainties are calculated using a generalized least square (GLS) approach available in the TEMPO and TEMPO2 software packages. Furthermore we also run a Markov Chain Monte Carlo (MCMC; similar to Lentati et al. 2014; Vigeland & Vallisneri 2014) analysis that simultaneously includes the noise parameters (See Section 3.1) and the nonlinear timing model. As shown in Table 3 and Figure 5, the results from this analysis are very consistent with the GLS approach, indicating that the assumption of linearity holds over the full timing parameter range.

Using a new noise modeling technique, we detected a significant red noise signal that could be the same "timing noise" described in Splaver et al. (2005). We also detected for the first time a change in the observed orbit period. The new timing model parameters (Tables 2 and 3) changed slightly from those in Splaver et al. (2005) but are consistent within their reported uncertainties.

3.1. Noise Model

The noise model used in this analysis is a parameterized model that is a function of several unknown quantities describing both correlated and uncorrelated noise sources. Uncorrelated noise is independent from one TOA to another, while the correlated noise is not. For instance, the template matching error mostly due to radiometer noise are uncorrelated in time, but the pulse jitter noise (Cordes & Shannon 2010), which affects the multi-frequency TOAs measured simultaneously across the band, is correlated in time. There is also time-correlated noise, such as red timing noise that is correlated from epoch to epoch. Among the various types of noise only the template matching error σ can be estimated when we compute the TOAs. Other sources of noise must be modeled separately. The solution to this problem has been discussed extensively in van Haasteren & Levin (2013), Ellis (2013), van Haasteren & Vallisneri (2014, 2015), Arzoumanian et al. (2014), and J. A. Ellis (PhD thesis 2014). In this section, we summarize the noise model used in this analysis (see, e.g., Arzoumanian et al. 2015, for more details).

To model uncorrelated noise, we use the standard EFAC and EQUAD parameters for each backend/receiver system (e.g., PUPPI backend with L-band receiver). These parameters simply re-scale the original TOA uncertainties

$$\sigma_{i,k} \rightarrow E_k\left(\sigma_{i,k}^2 + Q_k^2\right)^{1/2}, \tag{1}$$

where E_k and Q_k denote the EFAC and EQUAD parameters, respectively, and the subscript i is the TOA number and the subscript k denotes the backend/receiver system.

To model correlated noise we use the new ECORR parameter and a power-law red noise spectrum. The ECORR term describes short timescale noise that is completely correlated for all TOAs in a given observation but completely *uncorrelated* between observations. This term could be described as pulse phase jitter (Cordes & Shannon 2010) but could also have other components. The ECORR term manifests itself as a block diagonal term in the noise covariance matrix where the size of the blocks is equal to the number of TOAs in a given observation. The exact details of the implementation are described in Arzoumanian et al. (2015); however, the term essentially acts as a observation-to-observation variance. Finally, we model the red noise as a stationary Gaussian

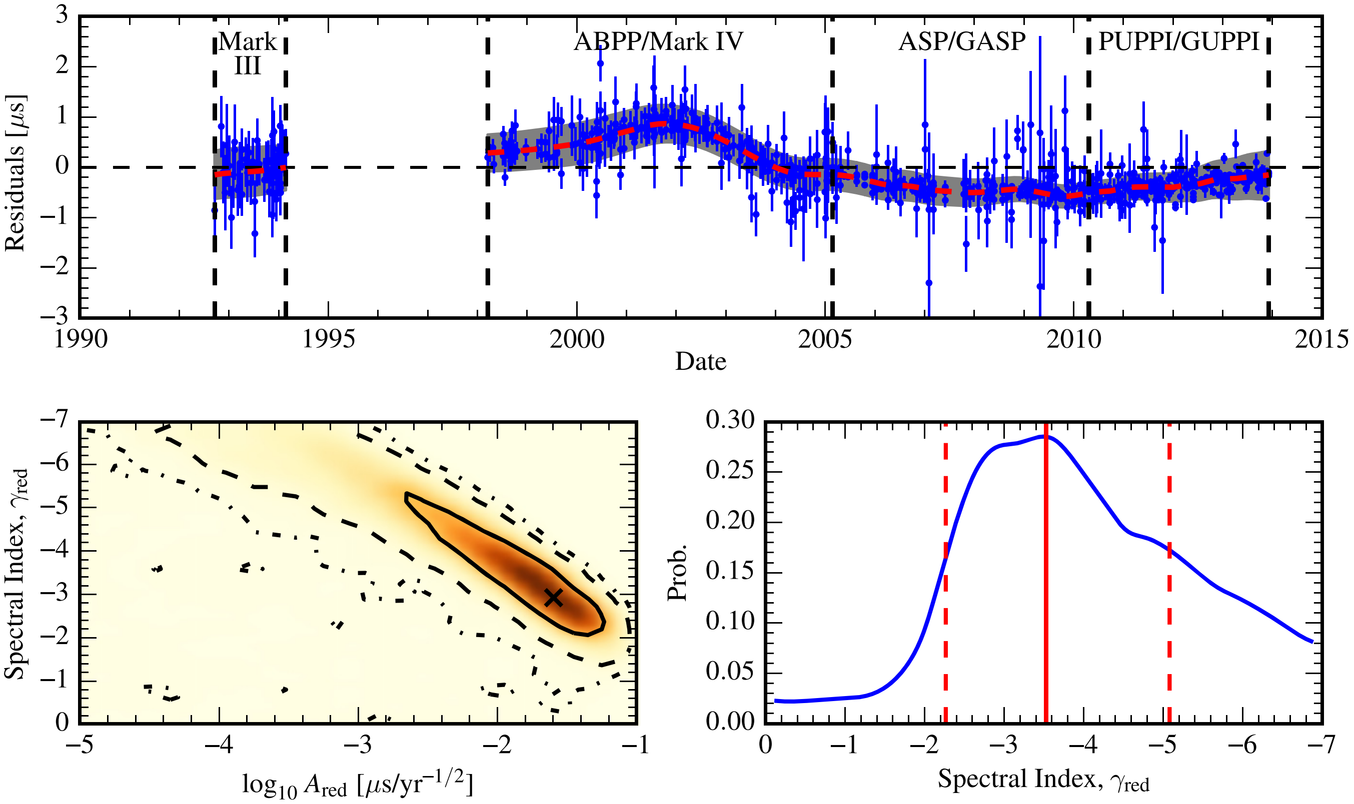

Figure 1. Top panel: daily averaged residuals of J1713+0747 produced from a GLS that includes a full noise model. The red dashed line and the gray shaded area show the maximum likelihood red noise realization and one-sigma uncertainty. The thick dashed vertical lines separate out various generations of backends used at both AO and GBT. Bottom left panel: two-dimensional marginalized posterior probability plot of red noise spectral index vs. logarithm of the red noise amplitude where the solid, dashed and dashed–dotted lines represent the 50%, 90%, and 95% credible regions. The "*x*" denotes the maximum likelihood value of the spectral index and amplitude. Bottom right panel: one-dimensional marginalized posterior probability for the red noise spectral index where the solid line denotes the maximum marginalized a-posteriori value and the dashed lines denote the 68% credible interval. Note that the 1D maximum marginalized posterior spectral index usually differs slightly from the global maximum likelihood value (−2.92) due to correlations with other parameters.

process that is parameterized by a power spectrum of the form

$$P(f) = A_{\rm red}^2 \left(\frac{f}{f_{\rm yr}}\right)^{\gamma_{\rm red}}, \qquad (2)$$

where $A_{\rm red}$ is the amplitude of the red noise in μs year$^{1/2}$ and $\gamma_{\rm red}$ is the spectral index.

These noise parameters are included in a joint likelihood that contains all timing model parameters. For the purposes of noise modeling, we analytically marginalize over the linear timing model parameters and explore the space of noise parameters via MCMC. We then use the MCMC results to determine the maximum likelihood noise parameters which are subsequently used as inputs to TEMPO/TEMPO2 GLS fitting routines. In our noise model we include EFAC, EQUAD, and ECORR parameters for data collected by different backend and receiver systems. However, we do not model EFAC and ECORR of the Mark III, Mark IV, and ABPP data because there were not enough TOAs in the legacy data set to constrain both EFAC and EQUAD. Furthermore, there was only one TOA per observation so we cannot constrain the observation-correlated noise modeled by ECORR. Instead, we set EFAC values to 1 and ECORR to 0 for these data sets, and use only EQUAD to model the white noise in these observations. The maximum likelihood values of the white noise parameters are presented in Table 4.

Shannon & Cordes (2012) studied the pulse arrival times from a single long exposure of PSR J1713+0747, and found that this pulsar's single pulses showed random jitter of $\simeq 26\ \mu$s. A similar result of $\simeq 27\ \mu$s was found by Dolch et al. (2014) from a more recent study using a 24 hr continuous observation of PSR J1713+0747 conducted with major telescopes around the globe. Therefore, by averaging many pulses collected in the typical ~20 minutes NANOGrav observation, one expects $\sim 27\ \mu{\rm s}/\sqrt{1200\nu} = 51$ ns of jitter noise. Tables 2 and 3 show the best-fit timing parameters before and after we applied our noise model to the data. It is clear that the jitter-like observation-correlated noise affected the arrival time of the pulses, such that some timing parameters changed significantly after including the jitter model. The optimal jitter parameters (ECORR, as shown in Table 4) from our noise modeling are mostly consistent with the prediction from Shannon & Cordes (2012), with some of them being higher. This could be due to the covariance between the jitter parameters and the EQUAD parameters.

In Figure 1 we show the red noise realization based on our best noise model (Table 4) and compare it to the post-fit residuals of a TEMPO GLS fit. The bottom panels of Figure 1 show the one- and two-dimensional posterior probability plots of the red noise. This noise model describes the data well as we can see in Figure 2 in which the maximum likelihood realizations of red and jitter noise are subtracted out. We see from the figure that both the high and low frequency residuals

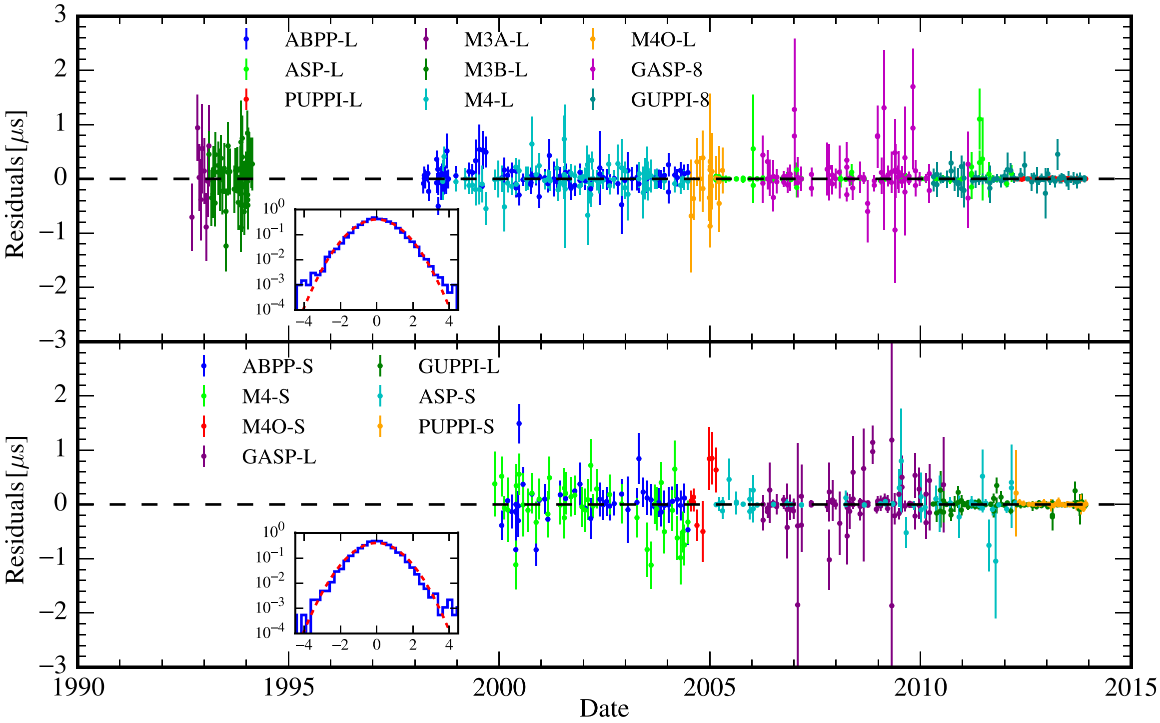

Figure 2. Top panel: low-frequency daily averaged residuals of J1713+0747 with maximum likelihood jitter and red noise realization subtracted out. Bottom panel: high-frequency daily averaged residuals of J1713+0747 with maximum likelihood jitter and red noise realization subtracted out. The insets in both top and bottom panels show the histogram of the weighted residuals (weighted by EFAC and EQUAD corrected TOA uncertainties) in logarithmic scale in blue curves, along with a zero-mean unit-variance Gaussian distribution marked as red dashed curves.

(with red and jitter noise realizations subtracted) are white (described by our EFAC and EQUAD parameters) and the weighted residuals follow a zero-mean unit-variance Gaussian distribution. We do note that the normalized residuals do not seem to follow exactly the Gaussian distribution outside of the 3σ range, this affects only $\lesssim$0.3% of the TOAs and will not significantly affect the results presented here.

Red noise was previously reported for PSR J1713+0747 by Splaver et al. (2005), who modeled it using an eighth-order polynomial. The largest residual in the present data set appears in the time period 1999–2005 (Figure 1). This is when dual-frequency observations begin, and it is likely that the red noise model is absorbing unmodeled DM variations in singe-frequency data collected before 1999, thus making physical interpretations of red noise difficult.

We reanalyzed the Splaver et al. (2005) data sets (Mark III, Mark IV, and ABPP data) with the new red noise modeling technique, and show that the timing results from the new method are mostly consistent with those from Splaver et al. (2005), except for α, δ, ν, and $\dot{\nu}$, which probably changed due to the new red noise model, and Keplerian parameters, which probably changed due to the fact that we used TEMPO2's T2 model instead of TEMPO's DD model used by Splaver et al. (2005). We fit the Keplerian and post-Keplerian parameters simultaneously using the T2 model, whereas Splaver et al. (2005) fit only for the Keplerian parameters while holding the post-Keplerian parameters to their best-fit values using the DD model. Therefore, the uncertainties reported in Splaver et al. (2005) do not reflect the covariance between the two sets of parameters but ours do.

The red noise signal found by our noise model applied to the Splaver et al. (2005) data set is consistent with that found in the 21 year data set, both in terms of the noise parameters (Tables 2, 3, and 5), and in terms of the shapes of the red noise realization (Figure 1), while the red noise modeled by high-order frequency polynomials varies significantly depending on the order of the polynomial or and the observation time span.

3.2. DM Variation

The DM of a pulsar reflects the number of free electrons between the pulsar and the telescopes and it varies because our sight-line through the turbulent ISM and solar wind is changing as the pulsar, the Sun, the Earth, and the ISM all move with respect to each other. DM variation can affect the timing of high-precision pulsars significantly.

We fit simultaneously with other parameters the time-varying DM using the *DMX* model in TEMPO. This model fits independent DM values for TOA groups taken within 14 day intervals, except for the L-band-only Mark III TOAs. We grouped the Mark III TOAs together as a single group, because their frequency resolution and timing precision are not sufficient for measuring epoch-to-epoch DM changes.

We turned off the solar wind model for TEMPO and TEMPO2 by setting the solar wind electron density (at 1 AU from the Sun) parameter n_0 to $0\,\mathrm{cm}^{-3}$ (the default value is $10\,\mathrm{cm}^{-3}$), and used the DMX model to model all DM variations including contribution from solar wind.

Figure 3 shows the measured DM variation of PSR J1713+0747. The sudden dip and recovery of DM around 2008 (MJD 54800) is due to changes either in the ISM or in the solar wind. This DM dip is also observed independently by the Parkes observatory (Keith et al. 2013) and the European Pulsar Timing Array (G. Desvignes et. al. 2015, in preparation).

Spectrum analysis of the time variation of flux, pulse arrival phase, and DM have been employed to study the turbulent

Table 5
The Timing Results from Splaver et al. (2005) and from a Re-analysis of the Splaver et al. (2005) Data Set Using New Red Noise Analysis Technique

Parameter	Splaver et al. (2005)	Red Noise Model[a]
R.A., α (J2000)	17:13:49.5305335(6)	17:13:49.5305321(6)
decl., δ (J2000)	7:47:37.52636(2)	7:47:37.52626(2)
Spin frequecy ν (s^{-1})	218.8118439157321(3)	218.811843915731(1)
Spin down rate $\dot{\nu}$ (s^{-2})	$-4.0835(2) \times 10^{-16}$	$-4.0836(1) \times 10^{-16}$
Proper motion in α, $\mu_\alpha = \dot{\alpha} \cos \delta$ (mas yr^{-1})	4.917(4)	4.917(4)
Proper motion in δ, $\mu_\delta = \dot{\delta}$ (mas yr^{-1})	−3.93(1)	−3.93(1)
Parallax, ϖ (mas)	0.89(8)	0.84(4)
Dispersion measure (pc cm^{-3})	15.9960	15.9940
Orbital period, P_b (day)	67.8251298718(5)[b]	67.825129921(4)
Change rate of P_b, $\dot{P}_b$ (10^{-12} s s^{-1})	0.0(6)	−0.2(7)
Eccentricity, e	0.000074940(1)[b]	0.000074940(1)
Time of periastron passage, T_0 (MJD)	51997.5784(2)[b]	51997.5790(6)
Angle of periastron, ω (deg)	176.192(1)[b]	176.195(3)
Projected semimajor axis, x (lt-s)	32.34242099(2)[b]	32.3424218(3)
Cosine of inclination, cos i	0.31(3)	0.32(2)
Companion mass, M_c ($M_\odot$)	0.28(3)	0.30(3)
Position angle of ascending node, Ω (deg)	87(6)	89(4)
Solar system ephemeris	DE405	DE405
Reference epoch for α, δ, and ν (MJD)	52000	52000
Pulsar mass, M_{PSR} ($M_\odot$)	1.3(2)	1.4(2)
Red noise amplitude (μs $year^{1/2}$)	⋯	0.004
Red noise spectral index	⋯	5.14

Notes.
[a] We used TEMPO2's *T2* binary model, which models the Keplerian (P_b, x, e, T_0, and ω) and post-Keplerian orbital elements (cos i, Ω, and m_2) simultaneously.
[b] Splaver et al. (2005) uses TEMPO's DD model and reports the uncertainties of the Keplerian parameters with the post-Keplerian ones fixed to their bestfit values.

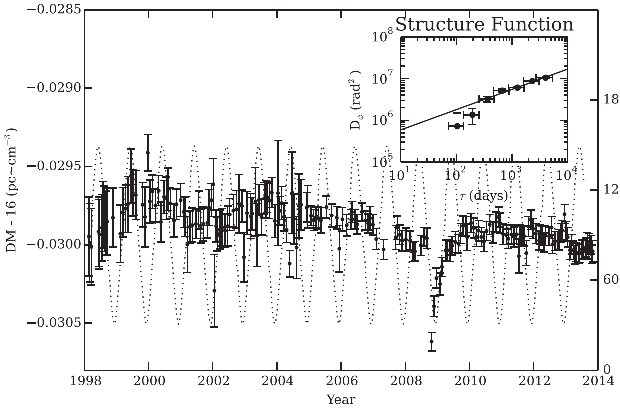

Figure 3. Plot shows 16-year DM variation of PSR J1713+0747. The dotted line shows the Solar elongation of the pulsar. The subplot shows the structure function (error bars) and its a power-law fit (solid line). The best-fit power-law index is 0.49(5), different from the value of 5/3 expected from a "pure" Kolmogorov medium.

nature of the ISM (e.g., Cordes et al. 1986; Rickett & Lyne 1990). It has been shown that DM variations of some pulsars are consistent with those expected from an ISM characterized by a Kolmogorov turbulence spectrum (Cordes et al. 1990; Rickett 1990; Kaspi et al. 1994; You et al. 2007; Keith et al. 2013; Fonseca et al. 2014). One can calculate the structure function of the varying DM:

$$D_\varphi(\tau) = \left(\frac{2\pi K}{f^2}\right)\langle[\mathrm{DM}(t+\tau) - \mathrm{DM}(t)]^2\rangle, \tag{3}$$

where τ is a given time delay, $K = 4.148 \times 10^3$ $\mathrm{MHz}^2\,\mathrm{pc}^{-1}\,\mathrm{cm}^3$ s, and f is the observing frequency in MHz. We expect, under the simplest assumptions, this function to follow a Kolmogorov power law $D_\varphi(\tau) = (\tau/\tau_0)^{\beta-2}$, where $\beta = 11/3$ and τ_0 is a characteristic timescale related to the inner scale of the turbulence. The pulsars with DM variations that fit this theory generally have large DM variations on timescale of years. However, PSR J1713+0747 does not show significant long-term DM variation (Figure 3). Conversely, it went through a steep drop and recovery around 2008. If such rapid DM changes are the result of variations in the ISM along the light of sight, such ISM variations do not fit the general characteristics of a Kolmogorov medium.

3.3. Pulsar Spin Irregularity

The term "timing noise" in pulsar timing generally refers to the non-white noise left in the timing residuals. An important contribution to timing noise is expected to come from the pulsar's spin irregularity, i.e., its long-term deviation from a simple linear slow down. Spin irregularity is often significant in younger pulsars, and may be modeled with high-order frequency polynomials (such as $\ddot{\nu}$, where ν is the pulsar's spin frequency). Potential causes of irregular spin behavior include unresolved micro-glitches, internal superfluid turbulence, magnetosphere variations, or external torques caused by matter surrounding the pulsar (Hobbs et al. 2010; Yu et al. 2013; Melatos & Link 2014). These mechanisms could lead to accumulative random perturbations in the pulsar's pulse phase, spin rate, or spin-down rate. Shannon & Cordes (2010) pointed out that one could model these types of timing noise using random walks. Random walks in phase (RW_0) would grow over time (T) proportionally to $T^{1/2}$, random walks in ν grow proportionally to $T^{3/2}$, random walks in $\dot{\nu}$ grow proportionally to $T^{5/2}$. Such spin noise would likely have a steep power spectrum with more power in the lower frequencies. This is considered as one of the main sources of "red" noise in pulsar timing.

The timing noise of radio pulsars has been studied by Cordes & Helfand (1980), Cordes & Downs (1985), Arzoumanian et al. (1994), D'Alessandro et al. (1995), Matsakis et al. (1997), and later by Hobbs et al. (2010) and Shannon & Cordes (2010) with large samples. Matsakis et al. (1997) adopted a generalized Allen Variance (traditionally used in measuring clock stability) to characterize the timing instability of pulsars:

$$\sigma_z(\tau) = \frac{\tau^2}{2\sqrt{5}} \langle c^2 \rangle^{1/2}, \tag{4}$$

where $\langle c^2 \rangle$ denotes the sum of squares of the cubic terms fitted to segments of length τ. Hobbs et al. (2010) found a best-fit scaling model of $\sigma_z(10\ \text{year})$ from a large sample of pulsars, including canonical pulsars (CPs) and MSPs:

$$\log_{10}\left[\sigma_z\left(10\ \ \text{year}\right)\right] = -1.37\,\log_{10}\left[\nu^{0.29}\left|\dot{\nu}\right|^{0.55}\right] + 0.52, \tag{5}$$

where ν, $\dot{\nu}$ are the pulsar's spin and spin-down rate. We find that Hobbs et al. (2010)'s scaling model ($\sigma^{\rm model}_{z,10\ \rm year} \simeq 1 \times 10^{-12}$) over-predicted $\sigma^{\rm measured}_{z,10\ \rm year} = 5 \times 10^{-16}$ for PSR J1713+0747 by more than three orders of magnitude.

Cordes & Helfand (1980) defined a different timing noise characteristic $\sigma^2_{\rm TN,2}$ based on the root mean square of residuals $\sigma^2_{\mathscr{R},2}$ from a timing fit that does not include any higher order spin parameters like $\ddot{\nu}$. The timing noise term is related to $\sigma^2_{\mathscr{R},2}$:

$$\sigma^2_{\mathscr{R},2}(T) = \sigma^2_{\rm TN,2}(T) + \sigma^2_W, \tag{6}$$

where σ^2_W is a time-independent term caused by white noise in the data. In this definition, timing noise $\sigma^2_{\rm TN,2}(T)$ grows bigger over time while white noise stays constant.

Shannon & Cordes (2010) studied the $\sigma^2_{\rm TN,2}$ from a large sample of CPs and MSPs. They found a scaling model:

$$\ln\left(\hat{\sigma}_{\rm TN,2}\right) = 1.6 - 1.4\ln(\nu) + 1.1\ln|\dot{\nu}_{-15}| + 2\ln\left(T_{\rm yr}\right), \tag{7}$$

where $\dot{\nu}_{-15}$ is $\dot{\nu}$ in units of $10^{-15}\ \text{s}^{-2}$, and $T_{\rm yr}$ is the observation time span in years. This scaling model predicts that, for 21-year timing of PSR J1713+0747, the residual rms without removing timing noise $\sigma^2_{\rm TN,2}$ would be ~400 ns. The measured rms of the red noise residual $\sigma^2_{\mathscr{R},\rm RN} = 364$ ns, is consistent with the extrapolation from Shannon & Cordes (2010). The best-fit scaling law also indicates that the residuals of the sampled pulsars $\hat{\sigma}_{\rm TN,2}$ seem to grow linearly with $T^2_{\rm yr}$. If the timing noise of the sampled pulsars is due to the accumulation of spin noise, and the spin noise is caused by the same physical processes, then this rms growth rate would imply that the spin noise of pulsars has a frequency power spectrum of power-law index $\gamma_{\rm red} \simeq -5$. This spectral index is consistent with the $\gamma_{\rm red}$ from our noise model. This can be seen in the bottom right plot of Figure 1 by noting that a spectral index of -5 is consistent with the posterior at the one-sigma level.

It is inconclusive whether or not the observed red noise can be interpreted as pulsar spin irregularity. Other sources of noise also could have contributed significantly. If we do assume that they are from spin irregularity, the estimated maximum likelihood red noise spectral index of ~ -3 favors that the pulsar spin irregularities come from random walks in either spin phase or spin rate, although other explanations cannot be ruled out due to the substantial uncertainty on the red noise spectral index (Figure 1).

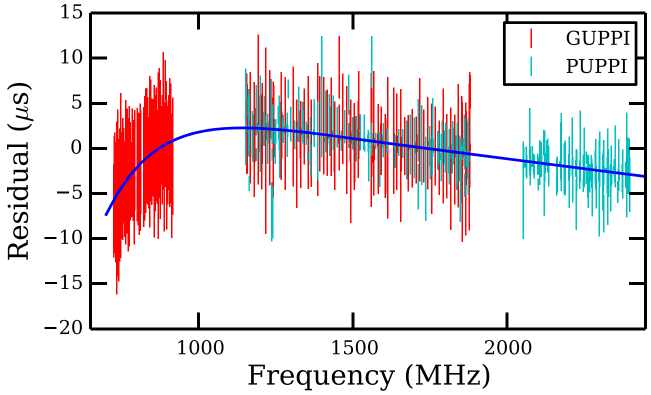

Figure 4. GUPPI and PUPPI post-fit residuals vs. frequency when fitted without the FD model, showing the frequency dependence of the TOAs that is not accounted for by the DM. For clarity, this plot is made using only TOAs with error smaller than 3 μs.

Finally, Shannon & Cordes (2010) showed that the significance of timing noise coming from gravitational wave (GW) background could be estimated as $\sigma_{\rm GW,2} \approx 1.3 A_0 (T_{\rm yr})^{5/3}$ ns, where A_0 is the characteristic strain at $f = 1\ \text{year}^{-1}$ and $T_{\rm yr}$ is the observational time span in years. The current best upper limit on GW characteristic strain is 2.4×10^{-15} (Shannon et al. 2013), which predicts an upper limit on timing noise of ~500 ns from GW background. Therefore, we cannot rule out the contribution of GWs in the timing noise.

3.4. *Pulse Profile Evolution with Frequency*

After removing the dispersion that causes TOA delays proportional to f^{-2}, where f is the observing frequency, we still see small remaining frequency-dependent residuals from wide-band observations using different instruments and telescopes (Figure 4). It appears that the low-frequency (~800 MHz) signals lead the high-frequency (1400 and 2300 MHz band) signals by microseconds. The cause of such TOA evolution is not clear. It could be a change in the pulsar's radiation pattern with frequency, or it could be the use of different standard profiles in different frequencies. Pulsar radiation of different frequencies may originate from different parts of the star's magnetosphere, and the radiation region of the pulsars' magnetosphere may be slightly distorted, leading to a frequency-dependent radiation pattern. Pennucci et al. (2014) and Liu et al. (2014) extensively discussed this phenomenon and developed TOA extraction techniques based on phase-frequency 2D pulse profile matching. This technique is not yet applied to our data set.

Demorest et al. (2013) allowed an arbitrary offset between TOAs taken with different observing systems and at different frequencies in order to model profile evolution with frequency. However, the number of frequency channels has increased by a factor of ten with the modern wide-band instruments, making it much harder to mitigate profile-frequency evolution using frequency channel offsets. Instead, we used the FD model, a polynomial of the logarithm of frequency: $\Delta t_{\rm FD} = \sum_{i=1}^{n} c_i (\log f)^i$ (Arzoumanian et al. 2015; solid line in Figure 4) to fit for and remove the profile-frequency evolution, where

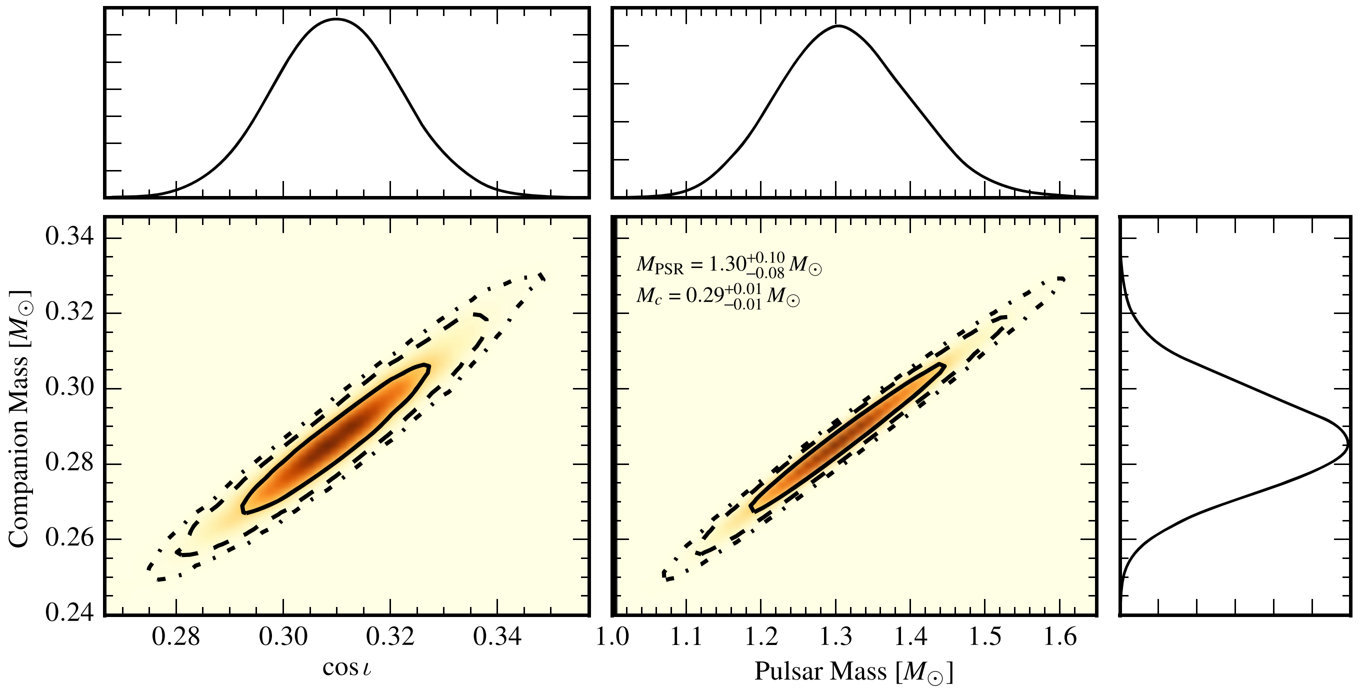

Figure 5. One- and two-dimensional posterior probability distributions of the cosine of the inclination angle, pulsar mass, and companion mass from the noise model MCMC including the full nonlinear timing model. The maximum marginalized posterior value and 1σ credible interval is very consistent with the GLS solution from TEMPO/TEMPO2. The solid, dashed, and dashed–dotted lines represent the 1σ, 2σ, and 3σ credible regions, respectively.

$\Delta t_{\rm FD}$ is the profile evolution term in units of seconds, f is the observing frequency in unit of GHz, and c_i are the FD model parameters. We employed an F-test with significance value of 0.0027 to determine how many FD parameters are needed to model profile frequency evolution. PSR J1713+0747 only requires $n = 4$ FD parameters.

4. RESULTS

4.1. Mass Measurements

The timing model of PSR J1713+0747 has been significantly improved by the 21-year timing effort. Most notably, the pulsar and the companion masses have been more precisely constrained (Tables 2 and 3, Figure 5) through Shapiro delay measurements. The companion's mass $M_{\rm c} = 0.286 \pm 0.012$ $M_\odot$ and the pulsar $M_{\rm PSR} = 1.31 \pm 0.11$ $M_\odot$ are in good agreement with the previously measured values (Splaver et al. 2005). Furthermore, we have carried out an MCMC run that uses the nonlinear timing model in order to map out any non-Gaussian correlations in parameter space. We find that the nonlinear model gives nearly identical results to the GLS method of TEMPO/TEMPO2. The covariance matrix used in our GLS fitting contains terms come from both the correlated and the uncorrelated noise; therefore, the timing parameter uncertainties we get have taken into account the contribution from the noise model. We note that, without the noise model, the derived pulsar masses would be substantially, and perhaps unrealistically, lower (with $\Delta M_{\rm PSR}$ ranges from 0.3 to 0.4 $M_\odot$) than the values with the noise model (Tables 2 and 3), suggesting that correlated noise would significantly impact the accuracy of high precision timing analysis.

The pulsar's mass is compatible with the distribution of pulsar masses in other neutron star-white dwarf systems, and in good agreement with the distribution of pulsar masses found in recycled binaries (Özel et al. 2012; Kiziltan et al. 2013). The precise measurement of neutron star masses may eventually help us understand the properties of matter of extreme density (Demorest et al. 2010; Lattimer 2012; Antoniadis et al. 2013).

In the standard picture of binary evolution, an MSP with a low-mass white dwarf companion must have been spun up through accretion when the white dwarf was a giant star filling its Roche lobe. This should lead to a strong correlation between the binary period and the mass of the white dwarf companion (Rappaport et al. 1995; Tauris & Savonije 1999; Podsiadlowski et al. 2002). Indeed, this picture has been supported by the measurements of several pulsar binary systems (e.g., Kaspi et al. 1994; van Straten et al. 2001; Ransom et al. 2014; Tauris & van den Heuvel 2014). The orbital period and companion mass of PSR J1713+0747 fit this correlation very well, thus supporting the standard MSP evolution theory.

4.2. Intrinsic Orbital Decay

We have observed an apparent change in orbital period from PSR J1713+0747, $\dot{P}_{\rm b} = (0.36 \pm 0.17) \times 10^{-12}$ s s^{-1} (Tables 2 and 3). This orbital period change is not intrinsic to the pulsar binary, but rather the result of the relative acceleration between the binary and the observer, i.e., the combination of differential acceleration in the Galactic gravitational potential (Damour & Taylor 1991) and the "Shklovskii" effect (Shklovskii 1970) which is caused by the transverse motion of the pulsar binary relative to Earth. We have good measurements of the distance and proper motion of the binary system, which allow us to remove these effects and study the system's intrinsic orbital decay.

The apparent change in orbital period due to differential acceleration in Galactic gravitational potential can be derived from

$$\dot{P}_{\rm b}^{\rm Gal} = \frac{A_{\rm G}}{c} P_{\rm b} = (-0.10 \pm 0.02) \times 10^{-12}\ {\rm s\ s^{-1}}, \tag{8}$$

where $A_{\rm G}$ is the line of sight acceleration of the pulsar binary. $A_{\rm G}$ is obtained using Equation (5) in Nice & Taylor (1995), Equation (17) in Lazaridis et al. (2009), the local matter density of Galactic disk around solar system (Holmberg & Flynn 2004) and the Galactic potential model by Reid et al. (2014).

The Shklovskii effect causes $P_{\rm b}$ to change by

$$\dot{P}_{\rm b}^{\rm Shk} = \left(\mu_{\alpha}^{2} + \mu_{\delta}^{2}\right) \frac{d}{c} P_{\rm b} = (0.65 \pm 0.02) \times 10^{-12}\ {\rm s\ s^{-1}}. \tag{9}$$

Therefore, the pulsar's intrinsic orbital decay is $\dot{P}_{\rm b}^{\rm Int} = \dot{P}_{\rm b}^{\rm Obs} - \dot{P}_{\rm b}^{\rm Shk} - \dot{P}_{\rm b}^{\rm Gal} = (-0.20 \pm 0.17) \times 10^{-12}\ {\rm s\,s^{-1}}$, and is consistent with zero.

Due to the very long ∼68 day orbit, the binary's decay due to the emission of gravitational radiation is expected to be undetectable: $\dot{P}_{\rm b}^{\rm GR} = -6 \times 10^{-18}\ {\rm s\,s^{-1}}$ (Lorimer & Kramer 2005). Therefore, the insignificant intrinsic orbital decay rate is entirely consistent with the description of quadrupolar gravitational radiation within General Relativity (GR).

Other than the gravitational radiation, two classical effects could have played a role in $\dot{P}_{\rm b}^{\rm Int}$. One, $\dot{P}_{\rm b}^{\dot{M}}$, is caused by mass loss in the binary system, and the other, $\dot{P}_{\rm b}^{\rm T}$, is the contribution from tidal effects. The pulsar and the white dwarf both could lose mass due to their magnetic dipole radiation; the maximum mass loss rate due to this effect can be estimated from the star's rotational energy loss rate. In the case of the pulsar, $\dot{M}_{\rm PSR} = \dot{E}/c^{2}$, which is measurable through the spin down rate of the pulsar. The white dwarf generally loses mass at a much lower rate than the pulsar. Therefore, orbital change due to mass loss can be estimated as $\dot{P}_{\rm b}^{\dot{M}} \sim 1 \times 10^{-14}\ {\rm s\,s^{-1}}$ (Damour & Taylor 1991; Equations (9) and (10) of Freire et al. 2012b). This is an order of magnitude smaller than the measured uncertainties on $\dot{P}_{\rm b}^{\rm Int}$. The tidal effect in this binary system is expected to be $\dot{P}_{\rm b}^{\rm T} \ll 3 \times 10^{-14}\ {\rm s\,s^{-1}}$ based on the most extreme scenarios (the white dwarf spins at its break-up velocity and the tidal synchronizing timescale equals the characteristic age of the pulsar; see Equation (11) in Freire et al. 2012b and references therein). Both of these extra terms are much smaller than the observed uncertainties on $\dot{P}_{\rm b}^{\rm Int}$.

4.3. Time Variation of G

Based on the measurement of "excess" orbital period change $\dot{P}_{\rm b}^{\rm exc} = \dot{P}_{\rm b}^{\rm Int} - \dot{P}_{\rm b}^{\dot{M}} - \dot{P}_{\rm b}^{\rm T} - \dot{P}_{\rm b}^{\rm GR}$, Damour et al. (1988) derived a phenomenological limit for $\dot{G}$ without considering the binding energy of the stars: $\dot{G}/G \simeq -\dot{P}_{\rm b}^{\rm exc}/(2P_{\rm b}) = (1.0 \pm 2.3) \times 10^{-11}\ {\rm yr^{-1}}$ using the timing of binary PSR B1913+16. Since then $\dot{P}_{\rm b}^{\rm exc}$ of pulsar binaries, including PSR J1713+0747, have been used to constrain $\dot{G}/G$ (Kaspi et al. 1994; Nice et al. 2005; Deller et al. 2008; Lazaridis et al. 2009; Freire et al. 2012b). So far all pulsar observations show $\dot{G}/G$ consistent with being zero, with upper limits largely determined by the uncertainties in orbital period change rate, distance, and proper motions. PSR J1713+0747 has the smallest known $\dot{P}_{\rm b}^{\rm exc}/(2P_{\rm b}) \simeq (-0.5 \pm 0.9) \times 10^{-12}\ {\rm yr^{-1}}$ (Section 4.2) and is particularly useful for constraining the time variability of the gravitational constant.

Nordtvedt (1990), Lazaridis et al. (2009), and Freire et al. (2012b) showed that a generic test of $\dot{G}/G$ can be achieved using pulsar binaries in a more rigorous fashion by incorporating the binding energy of the neutron stars. The binding energy of a compact star changes with the G, resulting in a changing mass, this will also affect the binary orbit. In a generic form, we could characterize this effect using a self-gravity "sensitivity" parameter s_p (Will 1993). The changing G will now change the orbital period of a pulsar binary system (Nordtvedt 1990; Lazaridis et al. 2009):

$$\dot{P}_{\rm b}^{\dot{G}} = -2\frac{\dot{G}}{G}\left[1 - \left(1 + \frac{m_c}{2M}\right)s_p\right]P_{\rm b}. \tag{10}$$

This formalism is more generic in the sense that it incorporates the compactness of the neutron star, but it also assumes that non-perturbative effects are absent and higher-order contributions in the self-gravity sensitivity can be neglected.

Meanwhile, in the framework of an alternative gravitation theory that violates SEP, a binary system may emit dipole gravitational radiation (Will 1993, 2001; Lazaridis et al. 2009; Freire et al. 2012b and references therein). Such effects arise when the two bodies are very different in terms of their self-gravity, i.e., their compactness. Under the aforementioned assumptions of neglecting non-perturbative effects and higher order contributions of self-gravity sensitivity, this extra dipole radiation could lead to an extra orbital change term:

$$\dot{P}_{\rm b}^{\rm D} \simeq -4\pi \frac{T_{\odot}\mu}{P_{\rm b}} \kappa_{\rm D} S^{2}, \tag{11}$$

(Will 1993; Lazaridis et al. 2009), where $T_{\odot} = GM_{\odot}/c^{3} = 4.925490947\mu{\rm s}$, μ is the reduced mass $(m_p m_c/M)$ of the system, $\kappa_{\rm D}$ is a dipole gravitational radiation "coupling constant," and S is the difference between the self-gravity "sensitivities" of the two bodies ($S = s_p - s_c$; $s_p \sim 0.1 m_{\rm p}/M_{\odot}$ according to Damour & Esposito-Farèse 1992; and $s_c \ll s_p$). In Einstein's GR $\kappa_{\rm D} = 0$—there is no self-gravity induced dipole gravitational radiation, but it is generally not the case in alternative theories that violate the SEP.

PSR J1713+0747 has a wider binary orbit than most other high-timing-precision pulsar binaries, making its $\dot{P}_{\rm b}^{\rm D}$ very small. Conversely, $\dot{P}_{\rm b}^{\dot{G}}$ is larger when $P_{\rm b}$ is large. This makes PSR J1713+0747 the best pulsar binary system for constraining the effect of the changing gravitational constant $\dot{G}$. Limits on both $\dot{G}$ and $\kappa_{\rm D}$ can be estimated in the same fashion as in Lazaridis et al. (2009): by solving $\dot{G}$ and $\kappa_{\rm D}$ simultaneously from the equation $\dot{P}_{\rm b}^{\rm exc} = \dot{P}_{\rm b}^{\rm D} + \dot{P}_{\rm b}^{\dot{G}}$ (Equation (29) of Lazaridis et al. 2009) of different pulsars. We applied this method to four pulsars: PSR J0437−4715, PSR J1012+5307, PSR J1738+0333, and PSR J1713+0747 using timing parameters reported in Lazaridis et al. (2009), Freire et al. (2012b), and this work. The resulting confidence region of $\dot{G}$ and $\kappa_{\rm D}$ is shown in Figure 6. We found, at 95% confidence limit, $\dot{G}/G = (0.6 \pm 1.1) \times 10^{-12}\ {\rm yr^{-1}}$; $\kappa_{\rm D} = (-0.9 \pm 3.3) \times 10^{-4}$. This constraint on $\dot{G}$ is more stringent than previous pulsar-based constraints (Freire et al. 2012b), and close to one of the best constraints of this type ($\dot{G}/G = (-0.07 \pm 0.76) \times 10^{-12}\ {\rm yr^{-1}}$) from the Lunar Laser Ranging (LLR) experiment (Hofmann et al. 2010), which measured Earth-moon distance to $\sim 10^{-11}$ precision through 39 years of laser ranging. Fienga et al. (2014) showed that $\dot{G}/G$

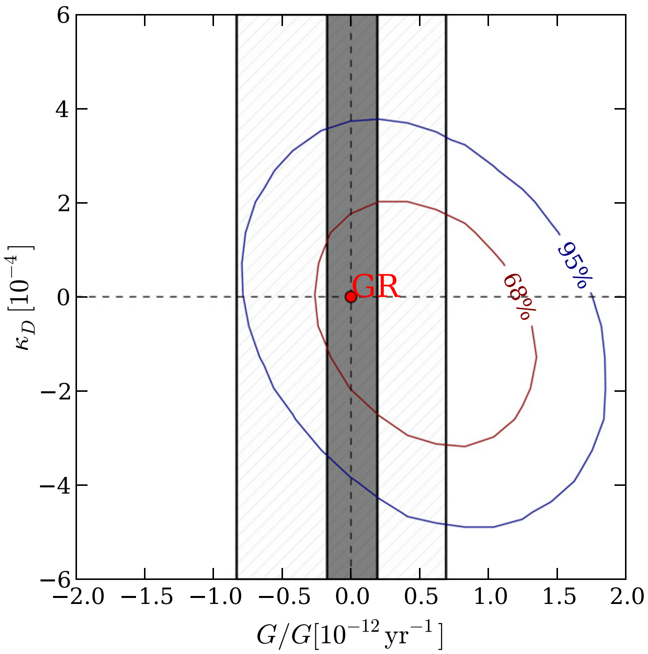

Figure 6. Confidence contour of $\dot{G}/G$ and κ_{D} calculated from PSRs J1012+5307, J1738+0333, and J1713+0747 using an MCMC simulation. The shaded area marks the 95% confidence $\dot{G}$ limit from LLR (Hofmann et al. 2010). The gray area marks the 95% confidence $\dot{G}$ limit from planetary ephemerides (Fienga et al. 2014).

can be constrained to $(0.01 \pm 0.18) \times 10^{-12}\,\mathrm{yr}^{-1}$ through the analysis of solar system planetary ephemerides. The κ_{D} limit, which is not constrained by solar-system tests, is also slightly improved by using PSR J1713+0747. The pulsar-timing $\dot{G}$ and κ_{D} limits are particularly interesting in the testing of SEP-violating alternative theories, because they arise from a test using objects of strong self-gravitation. For example, in some classes of the scalar-tensor theories, the effect of $\dot{G}/G$ could be significantly enhanced in pulsar-white dwarf binaries (Wex 2014).

4.4. SEP and PFE

The SEP states that the gravitational effect on a small test body is independent of its constitution, and in particular, that bodies of different self-gravitation should behave the same in the same gravitational experiments. This principle is violated in alternative theories of gravitation like the aforementioned Jordan–Fierz–Brans–Dicke scalar-tensor theory. The PSR J1713+0747 binary is an excellent laboratory for testing effects of SEP violation. If the SEP is violated, the neutron star and the white dwarf will be accelerated differently by the Galactic gravitational field, causing the binary orbit to be polarized toward the center of the Galaxy. The excess eccentricity is expected to be (Damour & Schäfer 1991):

$$|\boldsymbol{e}_F| = \frac{1}{2}\frac{\Delta\, g_\perp c^2}{\mathcal{FG}(M_{\mathrm{PSR}} + M_{\mathrm{c}})(2\pi/P_{\mathrm{b}})^2}, \tag{12}$$

where $\mathcal{F}$ is a factor accounts for potential changes in the periastron advance rate due to deviations from GR, $\mathcal{G}$ is the effective gravitational constant in the interaction between the pulsar and the white dwarf, and $g_\perp$ is the projection of Galactic acceleration on the orbital plane and Δ is the dimensionless factor that characterizes the significance of SEP violation. We assume $\mathcal{FG} \approx G$ here and after. The Galactic acceleration of the pulsar system is derived from Holmberg & Flynn (2004), Reid et al. (2014).

GR predicts that there is no preferred reference frame in the universe but this may be different in alternative theories. The Parameterized Post-Newtonian (PPN) formalism parameterized possible deviations from GR into a set of parameters (see Will 2014 for the list of them), some of which are associated with the PFE. In this work, we test α_3, one of the PFE-related parameters. If $\alpha_3 \neq 0$, this would lead to both the presence of a PFE and the breaking of momentum conservation. A rotating body would be accelerated perpendicular to its spin axis and its absolute velocity in the preferred reference frame. In a pulsar binary, this effect would cause an excess in eccentricity, which can be estimated by (Damour & Esposito-Farèse 1992; Bell & Damour 1996):

$$|\boldsymbol{e}_F| = \hat{\alpha}_3 \frac{c_p |\boldsymbol{w}| P_{\mathrm{b}}^2}{24\pi P} \frac{c^2}{\mathcal{FG}(M_{\mathrm{PSR}} + M_{\mathrm{c}})} \sin\beta, \tag{13}$$

where $\boldsymbol{w}$ is the absolute velocity of the binary system relative to the preferred frame of reference, typically taken as that of the cosmic microwave background (CMB), P is the pulsar's spin period, β is the angle between $\boldsymbol{w}$ and the spin axis of the pulsar, and $\hat{\alpha}_3$ is the strong-field version of the PPN parameters α_3. Here $\boldsymbol{w} = \boldsymbol{w}_\odot + \boldsymbol{v}_{\mathrm{PSR}}$, where $\boldsymbol{w}_\odot = 369 \pm 0.9\,\mathrm{km\,s^{-1}}$ is the velocity of the solar system relative to the CMB (Hinshaw et al. 2009), and the term $\boldsymbol{v}_{\mathrm{PSR}}$ is the relative speed of the pulsar to our solar system. $\boldsymbol{v}_{\mathrm{PSR}}$ is only partially known because we can measure the pulsar system's proper motion on the sky but we cannot measure its line-of-sight velocity (v_{r}).

Fortunately, many variables in these equations are measurable in the case of the PSR J1713+0747 binary. It is possible to constrain Δ and $\hat{\alpha}_3$ using Bayesian techniques by assuming certain fiducial priors for v_{r} (Splaver et al. 2005; Stairs et al. 2005; Gonzalez et al. 2011). In our case, we assumed a Gaussian prior for v_{r} centred at zero with a width equal to the system's proper motion speed. Based on our 21-year timing of J1713+0747 alone, we find 95% confidence limits on the violations of SEP and Lorentz invariance $\Delta < 0.01$ and $\hat{\alpha}_3 < 2 \times 10^{-20}$, slightly improving the single pulsar limits from earlier data on this pulsar (Splaver et al. 2005; Stairs et al. 2005; Gonzalez et al. 2011). Stronger limits can be found by combining the results from multiple similar pulsar systems (Wex 2000; Stairs et al. 2005; Gonzalez et al. 2011).

5. SUMMARY

In this paper, we present a comprehensive model of high precision timing observations of PSR J1713+0747 that spans 21 years. We improved measurements of the pulsar and its companion's masses and the shape and orientation of the binary orbit. We also detect, for the first time, an apparent change in orbital period due to Galactic differential accelerations and the Shklovskii effect. These measurements, when combined with those of other pulsars, significantly improve the pulsar timing limit on the rate of change of the gravitational constant, $\dot{G}$. Although the pulsar constraint is not better than the best solar system ones, it is nevertheless an independent test using extra-solar binary systems thousands of light-years away. The pulsar tests also could be more constraining for some classes of alternative gravitational theories that predict stronger non-GR effects in strong-field regime (Wex 2014). The new best pulsar timing limit on $\dot{G}/G$ is $(0.6 \pm 1.1) \times 10^{-12}\ \mathrm{yr}^{-1}$ ($<0.033H_0$ based on the 3-σ limit), where H_0 is the Hubble constant. In other words, the change rate of gravitational constant has to be a factor of at least 31 (3-σ limit) slower than the average expansion rate of the universe.

Meanwhile, the precise measurements of PSR J1713+0747's orbital eccentricity and 3D orientation allow us to test the violation of SEP and Lorentz invariance with it. We found a single-pulsar 95% upper limit on $\Delta < 0.01$, the SEP violation factor, and $\hat{\alpha}_3 < 2 \times 10^{-20}$, the PPN parameter that characterizes violation of Lorentz invariance. Because of the different statistical analysis methods used, our Δ and $\hat{\alpha}_3$ limits are slightly different but still consistent with the results of the same tests in previous publications (Wex 2000; Splaver et al. 2005; Stairs et al. 2005; Gonzalez et al. 2011; Freire et al. 2012a). Ultimately, the newly discovered pulsar triple system PSR J0337+1715 (Ransom et al. 2014) could yield the best test on SEP violation (Freire et al. 2012a; Berti et al. 2015; Shao et al. 2015). In this case the inner pulsar-white dwarf binary is orbited by another white dwarf in an outer orbit, making this system an excellent laboratory for testing the free fall of a neutron star and white dwarf in an external gravity field.

We studied the time variation of PSR J1713+0747's DM from 1998 to 2013, and fitted the structure function of the DM variation with a power law. The best-fit power law index is 0.49(5), significantly smaller than the 5/3 index expected from a "pure" Kolmogorov medium. This relatively flat structure function could be the result of either the lack of long-term DM variations or an excess of short-term variations. The sudden DM dip around 2008 (Figure 3) is a good example of such short-term DM variations. Similar non-Kolmogorov DM variations have been observed in some of the other NANOGrav pulsars (L. Levin et al. 2015, in preparation). Evidence of non-Kolmogorov behavior in the ISM was also found in the analysis of multi-frequency pulsar scatter times (Lewandowski et al. 2015).

As part of our timing modeling, we also included noise contribution such as jitter and red noise using the GLS fit and a covariance matrix that included the correlated and uncorrelated noise terms. We found that our timing result is significantly affected by the noise model, especially the jitter noise, suggesting that the adoption of jitter modeling may be necessary in other cases of high precision pulsar timing. We found that our noise parameters and timing residuals are consistent with the jitter noise estimates from Shannon & Cordes (2012) and the timing noise estimate from Shannon & Cordes (2010). However, the scaling law extrapolated from large sample studies of timing noise in Hobbs et al. (2010) overestimated the timing noise level $\sigma_z(10\ \mathrm{year})$ in this pulsar.

Our noise model parameters and timing residual rms (Table 4) provide a crude estimation of the amount of noise in our data. The weighted root mean square (WRMS; see Table 4 for definition) of the 21-year daily averaged timing residuals is ~92 ns. Table 4 shows a systematic improvement in the timing accuracy of this pulsar in the last two decades, due to advances in instrumentation. But the improvements are not as large as expected from the radiometer equation, perhaps because of pulse jitter.

Assuming that the red noise is caused by spin irregularity, the best-fit spectral index is consistent with spin irregularity caused by random walks in either the spin phase or the spin rate of the pulsar, but it does not exclude other explanations due to its large uncertainty (see bottom panel of Figure 1). The observed red noise level is also consistent with the prediction from the current best upper limit of GW background (Shannon et al. 2013), therefore, we cannot rule out significant timing noise contribution from the GW background.

The authors thank N. Wex, P. C. C. Freire, C. Ng, and J. Cordes for helpful comments and discussions. Pulsar research at UBC is supported by an NSERC Discovery Grant and Discovery Accelerator Supplement, and by the Canadian Institute for Advanced Research. J.A.E. acknowledges support by NASA through Einstein Fellowship grant PF4-150120. Some computational work was performed on the Nemo cluster at UWM supported by NSF grant No. 0923409. Portions of this research were carried out at the Jet Propulsion Laboratory, California Institute of Technology, under a contract with the National Aeronautics and Space Administration. T. Pennucci is a student at the National Radio Astronomy Observatory. The NANOGrav project receives support from the National Science Foundation (NSF) PIRE program award number 0968296. This work was supported by NSF grant 0647820. The Arecibo Observatory is operated by SRI International under a cooperative agreement with the National Science Foundation (AST-1100968), and in alliance with Ana G. Méndez-Universidad Metropolitana, and the Universities Space Research Association. The National Radio Astronomy Observatory (GBT) is a facility of the National Science Foundation operated under cooperative agreement by Associated Universities, Inc.

Facilities: Arecibo Telescope, Robert C. Byrd Green Bank Telescope.

REFERENCES

Antoniadis, J., Freire, P. C. C., Wex, N., et al. 2013, Sci, 340, 448
Arzoumanian, Z., Nice, D. J., Taylor, J. H., & Thorsett, S. E. 1994, ApJ, 422, 671
Arzoumanian, Z., Brazier, A., Burke-Spolaor, S., et al. 2014, ApJ, 794, 141
Arzoumanian, Z., Brazier, A., Burke-Spolaor, S., et al. 2015, in preparation
Backer, D. C., Dexter, M. R., Zepka, A., et al. 1997, PASP, 109, 61
Bell, J. F., & Damour, T. 1996, CQGra, 13, 3121
Berti, E., Barausse, E., Cardoso, V., et al. 2015, arXiv:1501.07274
Brans, C., & Dicke, R. H. 1961, PhRv, 124, 925
Camilo, F., Foster, R. S., & Wolszczan, A. 1994, ApJL, 437, L39
Chatterjee, S., Brisken, W. F., Vlemmings, W. H. T., et al. 2009, ApJ, 698, 250
Cordes, J. M., & Downs, G. S. 1985, ApJS, 59, 343
Cordes, J. M., & Helfand, D. J. 1980, ApJ, 239, 640
Cordes, J. M., Pidwerbetsky, A., & Lovelace, R. V. E. 1986, ApJ, 310, 737
Cordes, J. M., & Shannon, R. M. 2010, arXiv:1010.3785
Cordes, J. M., Wolszczan, A., Dewey, R. J., Blaskiewicz, M., & Stinebring, D. R. 1990, ApJ, 349, 245
D'Alessandro, F., McCulloch, P. M., Hamilton, P. A., & Deshpande, A. A. 1995, MNRAS, 277, 1033
Damour, T., & Deruelle, N. 1986, AnIHP, 44, 263
Damour, T., & Esposito-Farèse, G. 1992, CQGra, 9, 2093
Damour, T., Gibbons, G. W., & Taylor, J. H. 1988, PhRvL, 61, 1151
Damour, T., & Schäfer, G. 1991, PhRvL, 66, 2549
Damour, T., & Taylor, J. H. 1991, ApJ, 366, 501
Deller, A. T., Verbiest, J. P. W., Tingay, S. J., & Bailes, M. 2008, ApJL, 685, L67
Demorest, P. B. 2007, PhD thesis, Univ. California
Demorest, P. B., Pennucci, T., Ransom, S. M., Roberts, M. S. E., & Hessels, J. W. T. 2010, Natur, 467, 1081
Demorest, P. B., Ferdman, R. D., Gonzalez, M. E., et al. 2013, ApJ, 762, 94
Dirac, P. A. M. 1937, Natur, 139, 323
Dolch, T., Lam, M. T., Cordes, J., et al. 2014, ApJ, 794, 21
DuPlain, R., Ransom, S., Demorest, P., et al. 2008, Proc. SPIE, 7019, 70191D
Edwards, R. T., Hobbs, G. B., & Manchester, R. N. 2006, MNRAS, 372, 1549

Ellis, J. A. 2013, CQGra, 30, 224004
Ellis, J. A. 2014, PhD thesis, Univ. of Wisconsin-Milwaukee
Fienga, A., Laskar, J., Exertier, P., Manche, H., & Gastineau, M. 2014, arXiv:1409.4932
Fierz, M. 1956, AcHPh, 29, 128
Folkner, W. M., Williams, J. G., & Boggs, D. H. 2009, IPNPR, 178, C1
Fonseca, E., Stairs, I. H., & Thorsett, S. E. 2014, ApJ, 787, 82
Foster, R. S., Wolszczan, A., & Camilo, F. 1993, ApJL, 410, L91
Freire, P. C. C., Kramer, M., & Wex, N. 2012a, CQGra, 29, 184007
Freire, P. C. C., Wex, N., Esposito-Farèse, G., et al. 2012b, MNRAS, 423, 3328
Gonzalez, M. E., Stairs, I. H., Ferdman, R. D., et al. 2011, ApJ, 743, 102
Hinshaw, G., Weiland, J. L., Hill, R. S., et al. 2009, ApJS, 180, 225
Hobbs, G., Lyne, A. G., & Kramer, M. 2010, MNRAS, 402, 1027
Hobbs, G. B., Edwards, R. T., & Manchester, R. N. 2006, MNRAS, 369, 655
Hofmann, F., Müller, J., & Biskupek, L. 2010, A&A, 522, L5
Holmberg, J., & Flynn, C. 2004, MNRAS, 352, 440
Hotan, A. W., Bailes, M., & Ord, S. M. 2006, MNRAS, 369, 1502
Jordan, P. 1955, Schwerkraft und Weltall Grundlagen Der Theoretischen Kosmologie (Vieweg)
Jordan, P. 1959, ZPhy, 157, 112
Kaspi, V. M., Taylor, J. H., & Ryba, M. 1994, ApJ, 428, 713
Keith, M. J., Coles, W., Shannon, R. M., et al. 2013, MNRAS, 429, 2161
Kiziltan, B., Kottas, A., De Yoreo, M., & Thorsett, S. E. 2013, ApJ, 778, 66
Kopeikin, S. M. 1996, ApJ, 467, L93
Lattimer, J. M. 2012, ARNPS, 62, 485
Lazaridis, K., Wex, N., Jessner, A., et al. 2009, MNRAS, 400, 805
Lentati, L., Alexander, P., Hobson, M. P., et al. 2014, MNRAS, 437, 3004
Lewandowski, W., Kowalinska, M., & Kijak, J. 2015, arXiv:1502.06330
Liu, K., Desvignes, G., Cognard, I., et al. 2014, MNRAS, 443, 3752
Lommen, A. N., & Backer, D. C. 2001, ApJ, 562, 297
Lorimer, D. R., & Kramer, M. 2005, Handbook of Pulsar Astronomy (Cambridge: Cambridge Univ. Press)
Marciano, W. J. 1984, PhRvL, 52, 489
Matsakis, D. N., Taylor, J. H., Eubanks, T. M., & Marshall, T. 1997, A&A, 326, 924
McLaughlin, M. A. 2013, CQGra, 30, 224008
Melatos, A., & Link, B. 2014, MNRAS, 437, 21
Nice, D. J., Splaver, E. M., Stairs, I. H., et al. 2005, ApJ, 634, 1242
Nice, D. J., & Taylor, J. H. 1995, ApJ, 441, 429
Nordtvedt, K. 1990, PhRvL, 65, 953
Özel, F., Psaltis, D., Narayan, R., & Santos Villarreal, A. 2012, ApJ, 757, 55
Pennucci, T. T., Demorest, P. B., & Ransom, S. M. 2014, ApJ, 790, 93
Podsiadlowski, P., Rappaport, S., & Pfahl, E. D. 2002, ApJ, 565, 1107
Ransom, S. M., Stairs, I. H., Archibald, A. M., et al. 2014, Natur, 505, 520
Rappaport, S., Podsiadlowski, P., Joss, P. C., DiStefano, R., & Han, Z. 1995, MNRAS, 273, 731
Reid, M. J., Menten, K. M., Brunthaler, A., et al. 2014, ApJ, 783, 130
Rickett, B. J. 1990, ARAA, 28, 561
Rickett, B. J., & Lyne, A. G. 1990, MNRAS, 244, 68
Shannon, R. M., & Cordes, J. M. 2010, ApJ, 725, 1607
Shannon, R. M., & Cordes, J. M. 2012, ApJ, 761, 64
Shannon, R. M., Ravi, V., Coles, W. A., et al. 2013, Sci, 342, 334
Shao, L., Stairs, I. H., Antoniadis, J., et al. 2015, arXiv:1501.00058
Shklovskii, I. S. 1970, SvA, 13, 562
Splaver, E. M., Nice, D. J., Stairs, I. H., Lommen, A. N., & Backer, D. C. 2005, ApJ, 620, 405
Stairs, I. H., Splaver, E. M., Thorsett, S. E., Nice, D. J., & Taylor, J. H. 2000, MNRAS, 314, 459
Stairs, I. H., Faulkner, A. J., Lyne, A. G., et al. 2005, ApJ, 632, 1060
Stinebring, D. R., Kaspi, V. M., Nice, D. J., et al. 1992, RScI, 63, 3551
Tauris, T. M., & Savonije, G. J. 1999, A&A, 350, 928
Tauris, T. M., & van den Heuvel, E. P. J. 2014, ApJL, 781, L13
Taylor, J. H. 1992, RSPTA, 341, 117
van Haasteren, R., & Levin, Y. 2013, MNRAS, 428, 1147
van Haasteren, R., & Vallisneri, M. 2014, PhRvD, 90, 104012
van Haasteren, R., & Vallisneri, M. 2015, MNRAS, 446, 1170
van Straten, W., & Bailes, M. 2003, in Radio Pulsars, ed. M. Bailes, D. J. Nice & S. Thorsett (San Francisco, CA: ASP), 65
van Straten, W., Bailes, M., Britton, M., et al. 2001, Natur, 412, 158
Verbiest, J. P. W., Bailes, M., Coles, W. A., et al. 2009, MNRAS, 400, 951
Vigeland, S. J., & Vallisneri, M. 2014, MNRAS, 440, 1446
Wex, N. 2000, in IAU Coll. 177, Pulsar Astronomy—2000 and Beyond, ed. M. Kramer, N. Wex, & R. Wielebinski (San Francisco, CA: ASP), 113
Wex, N. 2014, arXiv:1402.5594
Will, C. 2001, LRR, 4, 4
Will, C. M. 1993, Theory and Experiment in Gravitational Physics (Cambridge: Cambridge Univ. Press)
Will, C. M. 2014, LRR, 17, 4
Wu, Y.-S., & Wang, Z. 1986, PhRvL, 57, 1978
You, X. P., Hobbs, G., Coles, W. A., et al. 2007, MNRAS, 378, 493
Yu, M., Manchester, R. N., Hobbs, G., et al. 2013, MNRAS, 429, 688